NANO LETTERS
Letter
Cite This: Nano Lett. 2018, 18, 4285−4292
pubs.acs.org/NanoLett

Strong Coupling of Epsilon-Near-Zero Phonon Polaritons in Polar Dielectric Heterostructures

Nikolai Christian Passler,*[,†] Christopher R. Gubbin,[‡] Thomas Graeme Folland,[§] Ilya Razdolski,[†] D. Scott Katzer,[∥] David F. Storm,[∥] Martin Wolf,[†] Simone De Liberato,[‡] Joshua D. Caldwell,[§,∥] and Alexander Paarmann*[,†]

[†]Fritz-Haber-Institut der Max-Planck-Gesellschaft, Faradayweg 4-6, 14195 Berlin, Germany
[‡]School of Physics and Astronomy, University of Southampton, Southampton SO17 1BJ, United Kingdom
[§]Vanderbilt Institute of Nanoscale Science and Engineering, 2301 Vanderbilt Place, PMB 350106, Nashville, Tennessee 37235-0106, United States
[∥]U.S. Naval Research Laboratory, 4555 Overlook Avenue SW, Washington, DC 20375, United States

Supporting Information

ABSTRACT: We report the first observation of epsilon-near-zero (ENZ) phonon polaritons in an ultrathin AlN film fully hybridized with surface phonon polaritons (SPhP) supported by the adjacent SiC substrate. Employing a strong coupling model for the analysis of the dispersion and electric field distribution in these hybridized modes, we show that they share the most prominent features of the two precursor modes. The novel ENZ-SPhP coupled polaritons with a highly propagative character and deeply subwavelength light confinement can be utilized as building blocks for future infrared and terahertz nanophotonic integration and communication devices.

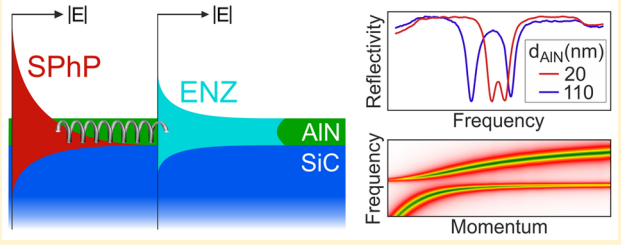

KEYWORDS: *Surface phonon polariton, epsilon-near-zero, infrared, nanophotonics, polar crystal, strong coupling, hybridization*

Integrated terahertz (THz) photonics relies on the development of artificially designed nanoscale metamaterials, where subwavelength structures in periodic patterns enable precise tuning of the material's optical response.[1−3] Truly extraordinary light propagation characteristics can be achieved in metamaterial-based epsilon-near-zero (ENZ) media,[4,5] that is, where the dielectric permittivity is vanishingly small. In particular, remarkable properties of the ENZ photonic modes include tunneling through narrow distorted channels,[6,7] enhanced nonlinear-optical conversion efficiency via enforced phase-matching,[8−10] high emission directionality,[11−13] and enable polaritonic waveguiding modes with broken time inversion symmetry and reduced scattering rate.[14,15]

An important challenge of future nanophotonics consists in enabling effective nanoscale communication and long-range information transfer. Both those objectives can be greatly facilitated by exploiting the unique properties of ENZ physics. In this regard, it is of key importance to find an appropriate class of systems where high-Q ENZ polaritons can be efficiently excited and coupled to other photonic excitations, while maintaining highly propagative character with reasonable group velocities. Commonly, bulk ENZ photonic modes excited in carefully designed metamaterials based on plasmonic nanostructures are considered, which are, however, characterized by high losses.[16,17] A complementary approach aims at utilizing the naturally occurring zero-crossing of the dielectric function in the spectral vicinity of intrinsic material vibrations, such as the transverse optical (TO) and longitudinal optical (LO) phonons in polar dielectric crystals.[18−20] Yet, employing freestanding films of polar dielectrics,[19] however, bears little practical importance, and the low dispersion results in a nonpropagative character of the ENZ polaritonic modes.[18]

In this work, we suggest a novel concept for ENZ excitations, which utilizes strong coupling between the ENZ and surface phonon polaritons (SPhPs) in the reststrahlen band of polar dielectrics (demarcated by the phonon frequencies ω_{TO} and ω_{LO}[21,22]). We demonstrate the hybridization of an ENZ polariton and a propagating low-loss SPhP at an adjacent interface in the strong coupling regime, thus adding a new pair of coupled nanophotonic excitations to an evergrowing suite.[23−27] We analyze the coupling of the ENZ and SPhP modes in an AlN/SiC bilayer, where the ENZ polariton in AlN occurs within the reststrahlen band of SiC. The novel coupled ENZ-SPhP modes inherit their properties from both ENZ and SPhP components, thus enabling highly efficient phase-matched excitation. Offering broad functionality, these ENZ-SPhP coupled modes feature a unique combination of deeply subwavelength confinement, large enhancements of the local electromagnetic fields, as well as

Received: March 29, 2018
Revised: May 30, 2018
Published: June 12, 2018

DOI: 10.1021/acs.nanolett.8b01273
Nano Lett. 2018, 18, 4285−4292

an intrinsically low-loss, propagative character with nonzero group velocity.

A SPhP mode supported at the interface of a polar dielectric in the Reststrahlen band is split into two branches upon reducing the film thickness d (Figure 1a), known as symmetric and antisymmetric modes.[18,19,28] Remarkably, in ultrathin films ($d/\lambda < 10^{-2}$ with λ being the free-space wavelength) the upper (symmetric) mode is pushed toward the LO phonon frequency,[18] where the real part of the dielectric permittivity approaches zero ($\varepsilon'(\omega = \omega_{LO}) = 0$). While this ultrathin film ENZ polariton loses its dispersive character, its ultralong wavelength leads to a strongly subwavelength mode confinement, enabling a gigantic enhancement of the electric field with minimal phase change over several times the free-space wavelength. The polariton dispersion curves in the bilayer with an ultrathin AlN film on top of a SiC substrate are exemplified in Figure 1b. Individually, the AlN film exhibits a nondispersive ENZ polariton mode (light blue) and the SiC a SPhP (dark blue), see Figure S1a of the Supporting Information. The combined bilayer structure (inset Figure 1b), however, reveals a strong interaction between the two modes, leading to two new dispersive branches featuring an avoided crossing (red).

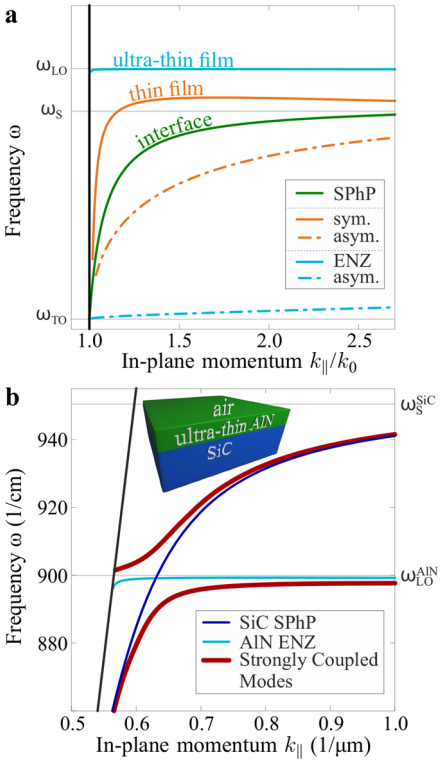

Figure 1. Interaction of a surface phonon polariton with an epsilon-near-zero mode. (a) A SPhP propagating at a single interface of air and a polar crystal has a dispersion relation (green curve) ranging from the transversal optical phonon frequency ω_{TO} up to a cutoff frequency ω_S, shown in green. For film thicknesses $d < \lambda/2$, where λ is the free-space wavelength, a symmetric and an antisymmetric branch appear (orange), splitting further apart with decreasing d. In the ultrathin limit of $d < \lambda/100$, the upper branch is pushed close to the longitudinal optical phonon frequency ω_{LO} (light blue), where the permittivity exhibits a natural zero-crossing. Therefore, the symmetric branch is termed an epsilon-near-zero mode. (b) When an ultrathin AlN film is placed on bulk SiC, the AlN epsilon-near-zero mode (light blue) intersects the SiC SPhP dispersion relation (dark blue). These modes strongly interact, inducing an avoided crossing and forming two new dispersion branches of the coupled system, drawn in red.

In the experiments, we realize phase-matched excitation of the coupled modes by employing the Otto prism geometry[29,30] with a schematic provided in Figure 2a. For total internal reflection inside the prism, the evanescent wave at the prism backside enables phase-matched excitation of the polariton modes in the sample. Spectroscopic reflectivity measurements with varied incidence angle allow for the mapping out of the polariton dispersion relation (for details on the experimental methods see Supporting Information Section 1). In our AlN/SiC structure, two polariton branches are present, and hence two resonance dips can be observed (Figure 2b), showing that the frequency splitting of the branches increases for thicker films. This trend is also evident in the experimental reflectivity maps and the transfer matrix calculations in Figure 3. Furthermore, our data reveal the anticipated avoided crossing in the dispersion of the interacting polariton modes, corroborating the strong coupling mechanism.

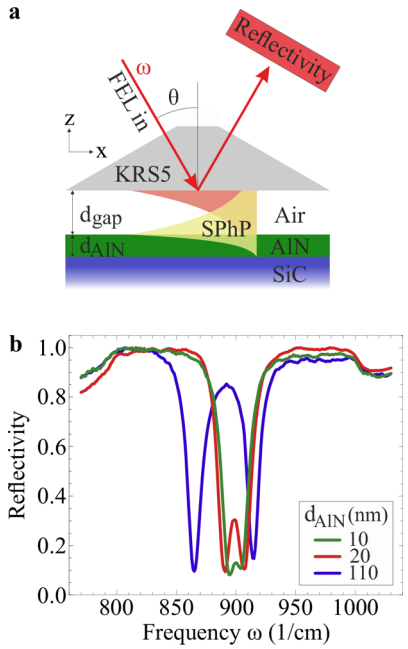

Figure 2. The variations of Rabi splitting for different AlN film thicknesses. (a) Prism coupling setup implementing the Otto configuration, where a highly refractive KRS5 prism ($n_{KRS5} \approx 2.4$) enables phase-matched excitation of phonon polaritons across a variable air gap. By tuning the incoming frequency ω and the incidence angle θ, polariton dispersion curves can be mapped out. (b) Reflectivity spectra for three different AlN film thicknesses d_{AlN} = 10, 20, 110 nm (θ = 29, 29, 30° and d_{gap} = 4.8, 4.5, 3.7 μm, respectively). The resonance dips represent the two strongly interacting polariton branches in the AlN/SiC heterostructure.

Analytically, the strong coupling can be described by a system of two coupled oscillators, modeling the ENZ and the SPhP modes, respectively. This allows us to calculate, in an analytically transparent way, the dispersion and the in-plane E-field distributions of the normal modes in the hybrid structure. The eigenfrequencies $\omega_q^{\pm}$ of the coupled system are then given by

DOI: 10.1021/acs.nanolett.8b01273
Nano Lett. 2018, 18, 4285−4292

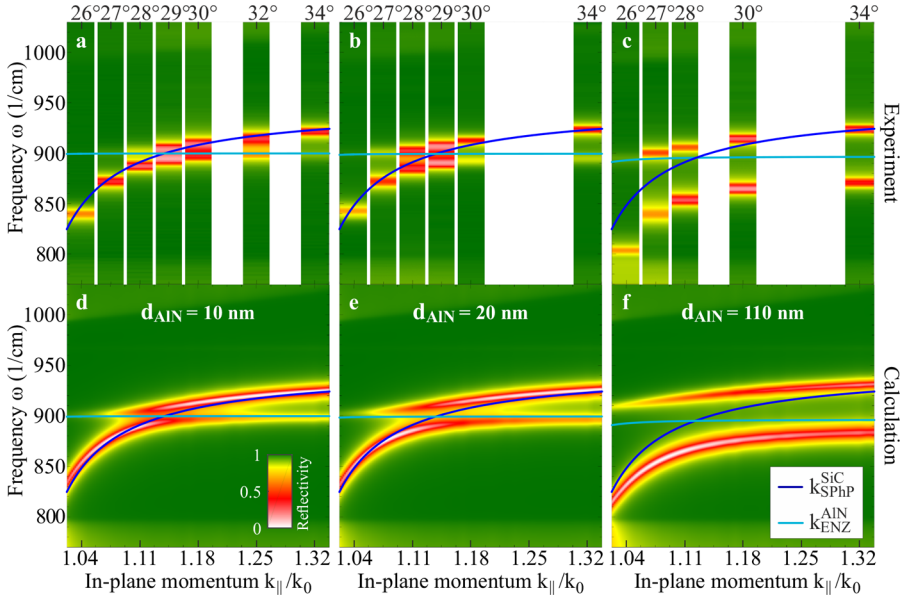

Figure 3. Mapping out the strongly coupled polariton dispersion. Experimental and calculated reflectivity maps for all three d_{AlN}, revealing the anticipated avoided crossing in the dispersion of the interacting polariton modes. The transfer matrix calculations (d–f) perfectly reproduce the experimental data (a–c). Clearly, the splitting of the modes is large for the thickest film and decreases for smaller thicknesses. The dark and light blue lines indicate the dispersion of the uncoupled SPhP and ENZ modes, respectively. The former is calculated in the limit of vanishing AlN thickness, while the latter is the dispersion of the ultrathin film polariton in a freestanding AlN film. We note that for the here shown film thicknesses, the dependence of the dispersion of the ultrathin film mode on d_{AlN} (compare to Figure 1a) is negligible.

$$\omega_q^{\pm} = \frac{\omega_q^e + \omega_q^s \pm \sqrt{(\omega_q^e - \omega_q^s)^2 + 4g_0^2}}{2} \quad (1)$$

where $\omega_q^{e,s}$ are the frequencies of the uncoupled ENZ and SPhP modes, respectively, and g_0 is the Rabi frequency, quantifying their mutual interaction. Although the eigenfrequencies in eq 1 can be derived using a classical coupled mode approach, as described in Methods, we decided to use instead the Hopfield model usually employed in solid-state cavity quantum electrodynamics,[31−34] which in our opinion allows us to gain a better insight into the hybrid nature of the resulting eigenmodes. We employ eq 1 to calculate the dispersion analytically (Figure 4a), finding excellent agreement of our strong coupling model with the numerical calculations and demonstrating that the description of the energetic hybridization of the modes in terms of strong coupling is correct.

Having established the strongly coupled oscillators model for the ultrathin AlN films on the SiC substrate, we now turn to its examination as a function of the AlN film thickness d_{AlN}. Two effects can be identified, which play an important role in the evolution of the strong coupling as d_{AlN} increases. First, because the SPhP is localized at the AlN/SiC interface and the ENZ mode in the entire AlN film, the spatial overlap of the two modes decreases, thus reducing the effective coupling strength. We can evaluate this through the distributions of the electric field calculated using the 4 × 4 transfer matrix formalism. These field distributions, exemplified for d_{AlN} = 110 nm in Figure S2c (see Supporting Information Section 4), indicate diminishing effective coupling strengths at $d_{AlN} \approx 50$ nm and beyond, while at smaller AlN thicknesses, this effect remains rather marginal, see Figure 4f. Second, because phonon polaritons are the collective excitations of atomic vibrations across individual bonds, increasing d_{AlN} in our model effectively results in a correspondingly larger oscillator strength f_{ENZ}. At these small thicknesses $d_{AlN} \ll \lambda$, the optical absorption scales almost linearly with thickness, leading to a concomitant linear increase of the oscillator strength. Within the strong coupling formalism, the Rabi frequency g_0 (determining half the distance between the two spectral peaks corresponding to the coupled modes) scales as $\sqrt{f_{ENZ}}$[35−37] and thus as $\sqrt{d_{AlN}}$. The Rabi frequency obtained from the fits of the calculated data using eq 1 follows this expected square root dependence with great accuracy, see Figure 4b. This behavior is further reproduced by the experimental coupling strengths also shown in Figure 4b, determined by half the frequency splitting in the respective reflectivity spectra (Figure 2b). Even though the Rabi frequency follows the $\sqrt{d_{AlN}}$ dependence up to $d_{AlN} \approx 500$ nm, the effective coupling strength is maximal for $d_{AlN} < 50$ nm due to the aforementioned loss of the spatial overlap of the two modes.

It is thus seen that the AlN/SiC bilayer can be tuned from the weak into the strong coupling regime by modifying the AlN layer thickness. In order to determine the lower limit of the d_{AlN} range of strong coupling, we employ the criterion which, quite intuitively, requires that the energy exchange rate between the two strongly coupled oscillators should exceed the loss rate, resulting in the appearance of two distinct frequencies in the spectrum.[38,39] A reliable and sufficient indication of the strong coupling is thus the avoided resonance crossing behavior (Figure 3) occurring if $2g_0/\gamma^* > 1$ is fulfilled, where $\gamma^* = (\gamma^e + \gamma^s)/2$ is the average of the loss rates of the two oscillators.

For our system, we obtain an estimate for the average loss rate of $\gamma^* = 5.8$. (While γ^s can be readily calculated using the transfer matrix method, determination of γ^e is not straightforward. As an estimation, we assume the proportionality of the loss rate γ to the imaginary part of the permittivity Im(ε) of the corresponding material where the mode is largely localized

DOI: 10.1021/acs.nanolett.8b01273
Nano Lett. 2018, 18, 4285−4292

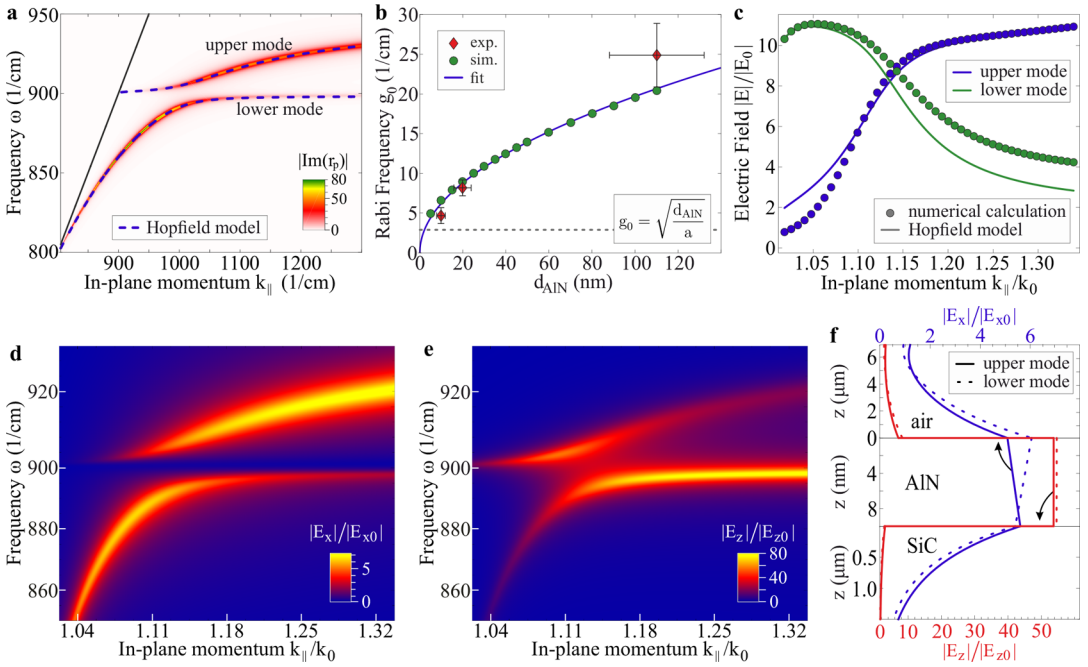

Figure 4. Coupling between the ENZ and SPhP modes. (a) Dispersion curves obtained by the analytical strong coupling model (dashed line) for an AlN film thickness of d_{AlN} = 10 nm on SiC on top of the numerically calculated dispersion curves obtained by computing the absolute imaginary part of the p-polarization reflection coefficient of the three layer system air/AlN/SiC. The analytical model features excellent agreement with the numerical calculations. (b) Rabi frequency g_0 as a function of d_{AlN} extracted from the analytical model (green circles) and experiments (red diamonds). As can be seen from the simple model fit (solid line, $a = 0.26 \times 10^{-13}$ m^3), the Rabi frequency follows a square root function characteristic for strong coupling. The dotted gray line indicates the threshold coupling strength for strong coupling according to the criterion discussed in the text. (c) Electric field strength obtained by the analytical model (solid line) and numerical calculations (circles) for the two strongly coupled modes, calculated at a probe point in air at the sample surface. At the avoided crossing, the two modes are completely hybridized, sharing equal field strength. At smaller in-plane momentum than at the avoided crossing, the lower branch has a larger field strength than the upper branch, and vice versa at larger momenta. The mode with larger field strength exhibits SPhP character because at the specific probe point the SPhP field dominates, whereas the ENZ polariton is localized inside the AlN film. (d,e) Normalized in-plane (E_x) and out-of-plane (E_z) field components along the entire dispersion. The SPhP has large in-plane and the ENZ polariton large out-of-plane fields, while the respective other component is small. This allows one to track the mode nature (SPhP or ENZ polariton) of both dispersion branches, which is exchanged at the avoided crossing, along the entire momentum range. (f) Normalized E_x and E_z fields of the upper and the lower mode at resonance ($k_\parallel/k_0$ = 1.13) across the air/AlN/SiC structure. The layer thicknesses are not to scale with respect to each other.

(AlN and SiC for the ENZ and SPhP modes, respectively). As such, at $\omega \approx 900$ cm^{-1} we get $\gamma^s \approx 8.7$ cm^{-1}, $\gamma^e \approx 3.0$ cm^{-1}, and thus $\gamma^* \approx 5.8$ cm^{-1}) The horizontal dotted line in Figure 4b illustrates the threshold coupling strength (2.9 cm^{-1}) corresponding to the onset of the strong coupling regime according to the aforementioned criterion. This value can be reached in AlN films with thicknesses of 2.2 nm. It is therefore seen that in the ultrathin AlN films on a SiC substrate discussed in this work, the ENZ and SPhP polaritons can indeed be strongly coupled for AlN film thicknesses 2.2 nm $\lesssim d_{AlN} \lesssim$ 50 nm.

Furthermore, our simple analytical model also correctly describes the electric field profiles. This is illustrated in Figure 4c, where we show the coinciding analytical and numerically calculated field intensities of both modes in front of the sample. We note that while a bare SiC substrate allows the SPhP component of the coupled modes to be quantified, the ENZ polariton component depends decisively on the substrate material and hence cannot be straightforwardly quantified. Therefore, we assumed the ENZ polariton to be fully confined in the AlN film, i.e., the field at the probe point is solely determined by the SPhP component of the coupled modes. This assumption is the reason for the discrepancy between the analytical and calculated field intensities at in-plane momenta where the respective mode features ENZ character ($k_\parallel/k_0 < 1.1$ and $k_\parallel/k_0 > 1.2$ in Figure 4c). However, despite its simplicity, our model reproduces the numerical field amplitudes extremely well, proving that the coupled modes can be described as a linear superposition of the ENZ and SPhP modes, weighted by the Hopfield coefficients. In consequence of this linear relationship, the strongly coupled modes at the avoided crossing share equal weights of SPhP and ENZ character, while the respective partitions change along the dispersion: the lower polariton starts as pure SPhP at small k and switches to ENZ beyond the avoided crossing, while the upper polariton shows the opposite behavior.

This switching of the mode nature can be illustrated by means of the in-plane (E_x) and out-of-plane (E_z) electric field components inside the AlN film, shown in Figure 4d,e, respectively. Note that the SPhP is characterized by a large in-plane field, whereas the ENZ polariton features pronounced out-of-plane field enhancement. The lower branch has strong in-plane fields at lower momentum (Figure 4d), illustrating that the mode is predominantly SPhP in nature. In contrast, the upper branch exhibits strong out-of-plane character at low $k_\parallel$ (Figure 4e). Across the strong coupling region, the modes interchange these characteristics with the upper branch exhibiting strong in-plane and the lower out-of-plane fields. At the avoided crossing, the fields of both modes are apparent and of equal weight, and even the spatial E_x and E_z field

DOI: 10.1021/acs.nanolett.8b01273
Nano Lett. 2018, 18, 4285−4292

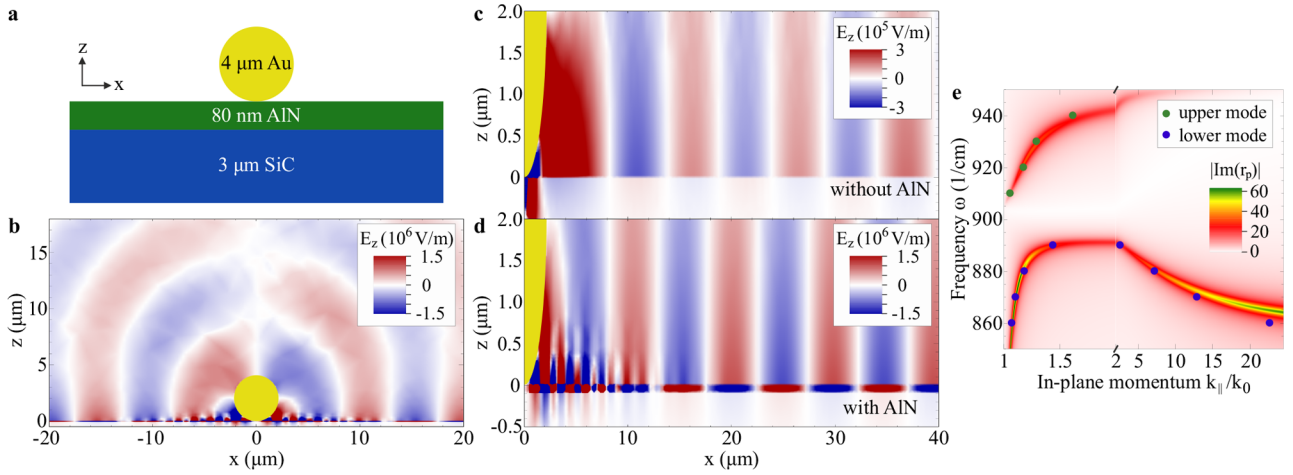

Figure 5. Numerical simulations of a high-k polariton with negative group velocity. (a) The simulation geometry, where plane waves are normally incident on a gold particle on the surface. Because of the large size of the particle, in (b) both surface waves and scattered free space waves are observed. (c,d) Surface electromagnetic field for a bare SiC substrate (c) and with an 80 nm AlN film on top (d). The field distributions in b–d were all calculated at an excitation frequency of 880 cm^{-1}. (e) Comparison between the dispersion relation calculated by a transfer matrix approach (background color map) and the values extracted from the simulations (circles). At large in-plane momentum ($k_\parallel/k_0 > 2$), the negative slope of the dispersion of the lower mode reveals its negative group velocity.

distributions of the modes across the multilayer structure show high agreement (Figure 4f). We have thus demonstrated the strong coupling and full hybridization of an ultrathin film ENZ phonon polariton with a SPhP in a polar dielectric heterostructure exemplified for AlN/SiC. However, we emphasize that strong coupling will emerge for a large number of hybrid systems that feature overlapping reststrahlen bands of the two constituents.[21,22] Furthermore, strong coupling can also be observed in the inverse structure of an ultrathin SiC film on AlN, occurring at the TO frequency of SiC (see Supporting Information Section 3).

Another important consideration which can be inferred from the distributions of the electric field is pertinent to the upper limit of the strong coupling. As mentioned above, for large thicknesses the spatial mismatch of the field distributions for the ENZ and SPhP modes (localized in the entire AlN film and at the AlN–SiC interface, respectively) becomes more and more important. For instance, in Supporting Information Section 4 the field distributions for the 110 nm thick AlN film are exemplified, clearly showing the lack of full hybridization of the ENZ and SPhP modes. Our calculations reveal that this effect becomes significant for thicknesses $d_{AlN} \gtrsim 50$ nm, thus reducing the effective coupling constant g_0. As such, we conclude that despite the fact that the mode splitting follows the $\sqrt{d_{AlN}}$ dependence up to $d_{AlN} \approx 500$ nm, ultrathin films with deeply subwavelength thicknesses of $d \sim \lambda/1000$ (11 nm for AlN) demonstrate the highest degree of strong coupling. In other words, within the strong coupling regime, thinner films provide higher quality ENZ wave characteristics, yet featuring full hybridization with the low-loss, highly confined SPhP, see Figure 4a–c. Within this regime, that is, for $d_{AlN} = 20$ nm, a propagation length of $L \approx 900$ μm with a group velocity of $v_g \approx 0.1$ c of the coupled modes is achieved. Thereby, the ENZ-SPhP modes offer a new promising approach for THz photonics on the nanoscale using traditional materials like III–V and II–VI semiconductors.[22] For instance, PbSe/PbS core–shell nanostructures[40] with wide tunability of the optical properties in the near-infrared additionally feature strongly coupled ENZ-SPhP modes in the THz range, allowing for a unique multispectral photonic integration.

To demonstrate that the general character of strong coupling is not restricted to the prism-based experiments, we complement our results with electromagnetic simulations of optical near-field scattering at nanoparticles. Motivated by previous results on scattering type scanning near field optical microscopy (s-SNOM) of Au nanostructures on SiC and boron nitride,[41,42] we consider here a Au cylinder on top of the AlN film on a SiC substrate, see Figure 5a. In the simulations, we monitor the spatial distribution of the electric field induced by normally incident plane waves at a series of frequencies. While an 80 nm AlN film was chosen in this simulation for a clear identification of the coupled polaritonic modes, similar results can be obtained for the AlN film thicknesses discussed earlier in this work.

Results for an 80 nm AlN film on top of a SiC substrate are presented in Figure 5b, showing the full electromagnetic field scattered from the Au cylinder at 880 cm^{-1}. To focus on the polaritons launched along the surface, in Figure 5c,d we consider the spatial distribution of the electric field along the surface in the two cases, namely, with and without the AlN layer. Without the AlN film (Figure 5c), the results of the simulations are indicative of a propagating SPhP wave launched across the surface with minimal confinement. In the presence of the AlN film, however, the simulations reveal two distinct modes with unequal wavelengths, see Figure 5d. The longer wavelength mode corresponds to that observed in our experiments, which is slightly compressed when compared with the wave propagating on the SiC surface. The short wavelength mode, however, was not observed in our measurements due to its large in-plane momentum. We attribute this mode to the breakdown of the thin film approximation for ENZ behavior which has been theoretically predicted at extremely large k.[18] One of the most striking features of this large-k mode is its negative group velocity, clearly visible from the dispersion in Figure 5e and confirmed by the time-dependent E-field distributions (Movie S1).

To better understand both the positive and negative group velocity modes observed in these simulations, we quantify the

DOI: 10.1021/acs.nanolett.8b01273
Nano Lett. 2018, 18, 4285–4292

polariton wavelength by Fourier transform (FT) of the simulated electromagnetic field. Here, we take the FT of the normal projection of the complex E_z field on the top surface of the AlN layer at a series of different excitation frequencies. The dispersion determined from the E_z Fourier spectra are plotted and compared against transfer matrix simulations of the polariton dispersion in Figure 5e. The excellent agreement between the numerically simulated frequencies and the calculated dispersion indicates that the key results of this paper regarding the spatial distribution of fields should be observable by the s-SNOM technique. Additionally, the latter should enable the observation of the high-k mode with negative dispersion, which is otherwise inaccessible in the prism-coupling experiments. We thus envisage rich perspectives of near-field microscopy in visualizing coupled phonon−polaritonic modes in hybrid or multilayer systems.

In conclusion, in this work we have demonstrated and characterized polaritonic modes in a strong coupling regime between an ENZ polariton and a bulk SiC SPhP in an ultrathin AlN/SiC structure. The full mode hybridization at the avoided crossing enables unique propagating ENZ polaritons. We have performed numerical simulations, revealing that the s-SNOM approach enables the observation of both the propagation length of the coupled ENZ-SPhP modes, and the properties of polaritons featuring negative group velocity. Our results illustrate the high suitability of near-field techniques like s-SNOM for the investigation of low-loss ENZ polaritons in polar dielectric heterostructures in order to further establish their potential for nanophotonic applications. We envision the generalization of employing polar dielectric ENZ heterostructures to open up a new platform of deeply subwavelength integrated THz photonics based on strongly coupled ENZ-SPhPs.

Methods. *Experimental Section.* The substrate of our samples is hexagonal 6H-SiC for the 110 nm AlN film, and 4H-SiC for the other two samples, all three with the extraordinary axis perpendicular to the sample surface (*c*-cut). The AlN layers were grown by RF-plasma assisted molecular beam epitaxy, and therefore also exhibit a *c*-cut, hexagonal crystal structure.

As an excitation source, we employ a mid-infrared free electron laser (FEL) with small bandwidth (~0.3%) and wide tunability of 3−50 μm, covering the spectral ranges of the SiC and AlN reststrahlen bands (details on the FEL have been reported elsewhere[43]). While the frequency is scanned by tuning the FEL, different in-plane momenta can be accessed via the incidence angle θ by rotating the entire Otto geometry (see Supporting Information Section 1 for more details), thus allowing for mapping out the complete dispersion curves experimentally.[30] In contrast to alternative approaches, the Otto geometry features experimental control over the excitation efficiency through tunability of the air gap width d_{gap}. At each incidence angle, spectra were taken at several d_{gap}. For the reconstruction of the dispersion curves (Figure 3), we selected the spectra at a gap size of critical coupling conditions d_{crit},[30] that is, where the polariton is excited the most efficiently (Supporting Information Section 2). Direct read-out of the gap width d_{gap} within a range of d = 1−50 μm is realized via whitelight interferometry, while the contrast of the interference spectrum grants parallel alignment of prism and sample.

Theoretical. Transfer Matrix. All calculations of the optical response and field distributions of Figures 1−4 were performed using a generalized 4 × 4 transfer matrix formalism.[44] In short, the formalism allows for the calculation of reflection and transmission coefficients in any number of stratified media with arbitrary dielectric tensor, which allows one to account for the anisotropy of our samples.

Three-Layer Dispersion. The dispersion curves in Figure 1 were obtained by numerical evaluation of the three-layer polariton dispersion formula[18,28,45]

$$1 + \frac{\varepsilon_1 k_{z3}}{\varepsilon_3 k_{z1}} = i \tan(k_{z2} d)\left(\frac{\varepsilon_2 k_{z3}}{\epsilon_3 k_{z2}} + \frac{\varepsilon_1 k_{z2}}{\varepsilon_2 k_{z1}}\right) \tag{2}$$

where the subscripts i = 1, 2, 3 correspond to the three stacked media, ε is the dielectric function, d is the film thickness of material 2, $k_{zi} = \sqrt{\frac{\omega}{c}\varepsilon_i - k_{\|}}$ is the out-of-plane momentum, and $k_{\|}$ is the in-plane momentum conserved in all layers.

Hopfield Model. In the rotating wave approximation, the two-oscillator Hopfield Hamiltonian for our system takes the form[31−34]

$$\mathcal{H} = \sum_q \hbar\omega_q^{e}\hat{a}_q^{\dagger}\hat{a}_q + \hbar\omega_q^{s}\hat{b}_q^{\dagger}\hat{b}_q + \hbar g_0(\hat{a}_q^{\dagger}\hat{b}_q + \hat{a}_q\hat{b}_q^{\dagger}) \tag{3}$$

where $\hat{a}_q^{\dagger}$ ($\hat{a}_q$) and $\hat{b}_q^{\dagger}$ ($\hat{b}_q$) are the bosonic creation (annihilation) operators for the ENZ and SPhP modes. The Rabi frequency g_0 of the strong coupling model in eq 3 is introduced as a phenomenological coupling parameter and is equivalent to the overlap of the substrate SPhP and ENZ polariton in a classical electromagnetic approach. The eigenfrequencies (eq 1) of the coupled system are found by diagonalization of the Hopfield-Bogoliubov matrix H_q[33]

$$H_q = \begin{pmatrix} \omega_q^{e} & g_0 \\ g_0 & \omega_q^{s} \end{pmatrix} \tag{4}$$

for each in-plane wavevector q individually, where e and s stand for the ENZ polariton and the substrate SPhP, respectively. The eigenvalues of these matrices yield the eigenfrequencies $\omega_q^{\pm}$ shown in eq 1, and the respective normalized eigenvectors (X_q, Y_q) are built from the Hopfield coefficients X_q and Y_q, describing the weighting factors of the ENZ polariton and the substrate SPhP which compose the two hybridized modes along the avoided crossing. The analytic electric field strength shown in Figure 4c has been calculated by multiplying these Hopfield coefficients with the electric field of the substrate SPhP at the probe point in air at the sample surface. The bosonic annihilation operators $\hat{p}_q$ of the coupled modes are then given by

$$\begin{aligned} \hat{p}_q^{+} &= X_q\hat{a}_q + Y_q\hat{b}_q \\ \hat{p}_q^{-} &= Y_q\hat{a}_q - X_q\hat{b}_q \end{aligned} \tag{5}$$

where the superscripts + and − denote the upper and the lower coupled polariton branch, respectively.

CST Simulations. Simulations for Figure 5 were performed in CST studio suite[46] using the frequency domain solver. To approximate the structure shown in Figure 5a within a finite 3D model, a unit cell with a size of 250 μm by 0.6 μm was chosen, which minimized nearest neighbor interactions. The optical constants of the respective materials were taken from literature.[47,48] Unit cell boundaries were used at the edges of the substrate, and a matched impedance layer was used to suppress substrate reflections. Fourier analysis was performed

DOI: 10.1021/acs.nanolett.8b01273
Nano Lett. 2018, 18, 4285−4292

using a one-dimensional field profile running along the top surface of the ENZ film down the center of the unit cell.

■ ASSOCIATED CONTENT

Supporting Information

The Supporting Information is available free of charge on the ACS Publications website at DOI: 10.1021/acs.nanolett.8b01273.

Experimental details (Section 1), critical coupling conditions of the strongly coupled modes (Section 2), strongly interacting modes in materials with overlapping reststrahlen bands (Section 3), deviation from strong coupling for larger film thicknesses (Section 4) (PDF)

Simulated time-dependent E-field distributions (Movie S1) (MPG)

■ AUTHOR INFORMATION

Corresponding Authors

*E-mail: passler@fhi-berlin.mpg.de.

*E-mail: alexander.paarmann@fhi-berlin.mpg.de.

ORCID

Nikolai Christian Passler: 0000-0002-7477-8611

Christopher R. Gubbin: 0000-0003-3988-028X

Joshua D. Caldwell: 0000-0003-0374-2168

Alexander Paarmann: 0000-0002-8271-2284

Notes

The authors declare no competing financial interest.

■ ACKNOWLEDGMENTS

We thank Wieland Schöllkopf and Sandy Gewinner for operating the FEL. D.S.K., D.F.S, and J.D.C. were supported by the Office of Naval Research through the U.S. Naval Research Laboratory and administered by the NRL Nanoscience Institute. The NRL team acknowledges the AlN characterization and processing contributions of Neeraj Nepal, Brian P. Downey, and Neil P. Green. S.D.L. is a Royal Society Research Fellow and he acknowledges support from the Innovation Fund of the EPSRC Programme EP/M009122/1.

■ REFERENCES

(1) Joannopoulos, J. D.; Johnson, S. G.; Winn, J. N.; Meade, R. D. *Photonic Crystals: Molding the Flow of Light*; Princeton University Press, 2008.

(2) Burgos, S. P.; De Waele, R.; Polman, A.; Atwater, H. A. *Nat. Mater.* **2010**, *9*, 407−412.

(3) Degl'Innocenti, R.; Kindness, S. J.; Beere, H. E.; Ritchie, D. A. *Nanophotonics* **2018**, *7*, 127−144.

(4) Li, Y.; Kita, S.; Muñoz, P.; Reshef, O.; Vulis, D. I.; Yin, M.; Lončar, M.; Mazur, E. *Nat. Photonics* **2015**, *9*, 738−742.

(5) Liberal, I.; Engheta, N. *Nat. Photonics* **2017**, *11*, 149−158.

(6) Silveirinha, M. G.; Engheta, N. *Phys. Rev. B: Condens. Matter Mater. Phys.* **2007**, *76*, 1−17.

(7) Edwards, B.; Al, A.; Silveirinha, M. G.; Engheta, N. *J. Appl. Phys.* **2009**, *105*, 044905.

(8) Argyropoulos, C.; Chen, P. Y.; D'Aguanno, G.; Engheta, N.; Alù, A. *Phys. Rev. B: Condens. Matter Mater. Phys.* **2012**, *85*, 1−5.

(9) Suchowski, H.; O'Brien, K.; Wong, Z. J.; Salandrino, A.; Yin, X.; Zhang, X. *Science* **2013**, *342*, 1223−1226.

(10) Mattiucci, N.; Bloemer, M. J.; D'Aguanno, G. *Opt. Express* **2014**, *22*, 6381.

(11) Enoch, S.; Tayeb, G.; Sabouroux, P.; Guérin, N.; Vincent, P. *Phys. Rev. Lett.* **2002**, *89*, 213902.

(12) Ziolkowski, R. W. *Physical Review E - Statistical, Nonlinear, and Soft Matter Physics* **2004**, *70*, 1−12.

(13) Kim, J.; Dutta, A.; Naik, G. V.; Giles, A. J.; Bezares, F. J.; Ellis, C. T.; Tischler, J. G.; Mahmoud, A. M.; Caglayan, H.; Glembocki, O. J.; et al. *Optica* **2016**, *3*, 339.

(14) Liu, R.; Roberts, C. M.; Zhong, Y.; Podolskiy, V. A.; Wasserman, D. *ACS Photonics* **2016**, *3*, 1045−1052.

(15) Engheta, N. *Science* **2007**, *317*, 1698−1702.

(16) Drachev, V. P.; Chettiar, U. K.; Kildishev, A. V.; Yuan, H.-K.; Cai, W.; Shalaev, V. M. *Opt. Express* **2008**, *16*, 1186−1195.

(17) Khurgin, J. B.; Boltasseva, A. *MRS Bull.* **2012**, *37*, 768−779.

(18) Campione, S.; Brener, I.; Marquier, F. *Phys. Rev. B: Condens. Matter Mater. Phys.* **2015**, *91*, 121408.

(19) Nordin, L.; Dominguez, O.; Roberts, C. M.; Streyer, W.; Feng, K.; Fang, Z. *Appl. Phys. Lett.* **2017**, *111*, 091105.

(20) Vassant, S.; Hugonin, J.-P.; Marquier, F.; Greffet, J.-J. *Opt. Express* **2012**, *20*, 23971.

(21) Caldwell, J. D.; Lindsay, L.; Giannini, V.; Vurgaftman, I.; Reinecke, T. L.; Maier, S. A.; Glembocki, O. J. *Nanophotonics* **2015**, *4*, 44−68.

(22) Feng, K.; Streyer, W.; Zhong, Y.; Hoffman, A.; Wasserman, D. *Opt. Express* **2015**, *23*, A1418.

(23) Caldwell, J. D.; Vurgaftman, I.; Tischler, J. G.; Glembocki, O. J.; Owrutsky, J. C.; Reinecke, T. L. *Nat. Nanotechnol.* **2016**, *11*, 9−15.

(24) Basov, D. N.; Fogler, M. M.; García De Abajo, F. J. *Science* **2016**, *354*, aag1992.

(25) Low, T.; Chaves, A.; Caldwell, J. D.; Kumar, A.; Fang, N. X.; Avouris, P.; Heinz, T. F.; Guinea, F.; Martin-Moreno, L.; Koppens, F. *Nat. Mater.* **2017**, *16*, 182−194.

(26) Simpkins, B. S.; Fears, K. P.; Dressick, W. J.; Spann, B. T.; Dunkelberger, A. D.; Owrutsky, J. C. *ACS Photonics* **2015**, *2*, 1460−1467.

(27) Dunkelberger, A. D.; Spann, B. T.; Fears, K. P.; Simpkins, B. S.; Owrutsky, J. C. *Nat. Commun.* **2016**, *7*, 13504.

(28) Burke, J. J.; Stegeman, G. I.; Tamir, T. *Phys. Rev. B: Condens. Matter Mater. Phys.* **1986**, *33*, 5186−5201.

(29) Otto, A. *Z. Phys. A: Hadrons Nucl.* **1968**, *216*, 398−410.

(30) Passler, N. C.; Razdolski, I.; Gewinner, S.; Schöllkopf, W.; Wolf, M.; Paarmann, A. *ACS Photonics* **2017**, *4*, 1048−1053.

(31) Hopfield, J. J. *Phys. Rev.* **1958**, *112*, 1555−1567.

(32) Savona, V.; Hradil, Z.; Quattropani, A.; Schwendimann, P. *Phys. Rev. B: Condens. Matter Mater. Phys.* **1994**, *49*, 8774−8779.

(33) Gubbin, C. R.; Martini, F.; Politi, A.; Maier, S. A.; De Liberato, S. *Phys. Rev. Lett.* **2016**, *116*, 1−6.

(34) Gubbin, C. R.; Maier, S. A.; De Liberato, S. *Phys. Rev. B: Condens. Matter Mater. Phys.* **2016**, *94*, 1−9.

(35) Lidzey, D. G.; Bradley, D. D. C.; Skolnick, M. S.; Virgili, T.; Walker, S.; Whittaker, D. M. *Nature* **1998**, *395*, 53−55.

(36) Cade, N. I.; Ritman-Meer, T.; Richards, D. *Phys. Rev. B: Condens. Matter Mater. Phys.* **2009**, *79*, 1−4.

(37) Baieva, S. V.; Hakala, T. K.; Toppari, J. J. *Nanoscale Res. Lett.* **2012**, *7*, 191.

(38) Auffèves, A.; Gerace, D.; Gérard, J. M.; Santos, M. F.; Andreani, L. C.; Poizat, J. P. *Phys. Rev. B: Condens. Matter Mater. Phys.* **2010**, *81*, 1−10.

(39) Rodriguez, S. R. K. *Eur. J. Phys.* **2016**, *37*, 025802.

(40) Lifshitz, E.; Brumer, M.; Kigel, A.; Sashchiuk, A.; Bashouti, M.; Sirota, M.; Galun, E.; Burshtein, Z.; Le Quang, A. Q.; Ledoux-Rak, I.; et al. *J. Phys. Chem. B* **2006**, *110*, 25356−25365.

(41) Huber, A. J.; Deutsch, B.; Novotny, L.; Hillenbrand, R. *Appl. Phys. Lett.* **2008**, *92*, 203104.

(42) Dai, S.; Ma, Q.; Yang, Y.; Rosenfeld, J.; Goldflam, M. D.; McLeod, A.; Sun, Z.; Andersen, T. I.; Fei, Z.; Liu, M.; et al. *Nano Lett.* **2017**, *17*, 5285−5290.

(43) Schöllkopf, W.; Gewinner, S.; Junkes, H.; Paarmann, A.; von Helden, G.; Bluem, H.; Todd, A. M. M. *Proc. SPIE* **2015**, *9512*, 95121L.

(44) Passler, N. C.; Paarmann, A. *J. Opt. Soc. Am. B* **2017**, *34*, 2128.

DOI: 10.1021/acs.nanolett.8b01273
Nano Lett. 2018, 18, 4285−4292

(45) Raether, H. *Surface Plasmons on Smooth and Rough Surfaces and on Gratings*; Tracts in Modern Physics; Springer, 1988; Vol. *111*.
(46) CST, CST Studio Suite. https://www.cst.com/products/csts2, (accessed May 07, 2018).
(47) Engelbrecht, F.; Helbig, R. *Phys. Rev. B: Condens. Matter Mater. Phys.* **1993**, *48*, 15698−15707.
(48) Moore, W. J.; Freitas, J. A.; Holm, R. T.; Kovalenkov, O.; Dmitriev, V. *Appl. Phys. Lett.* **2005**, *86*, 141912.

DOI: 10.1021/acs.nanolett.8b01273
Nano Lett. 2018, 18, 4285−4292